

# Tuning the composition of immiscible gold and nickel colloidal nanoalloys through plasmon induced laser mixing

Gabriele C. Messina<sup>1\*</sup>, Marco G. Sinatra<sup>2</sup>, Valentina Bonanni<sup>3,4</sup>, Rosaria Brescia<sup>5</sup>, Giulio Campo<sup>3</sup>, Francesco Pineider<sup>3,6</sup>, Claudio Sangregorio<sup>7</sup>, Giovanni Li-Destri<sup>8</sup>, Gianfranco Sfuncia<sup>9</sup>, Giovanni Marletta<sup>9</sup>, Alessandro Alabastri<sup>10</sup>, Remo Proietti Zaccaria<sup>1</sup>, Francesco De Angelis<sup>1</sup>, Giuseppe Compagnini<sup>2</sup>

1 Plasmon Nanotechnologies, Istituto Italiano di Tecnologia, Via Morego 30, 16163 Genoa, Italy

2 Laboratory for Thin Films and Nanostructures (LABFSN), Department of Chemical Sciences, University of Catania, Viale Andrea Doria 6, 95124 Catania, Italy

3 Department of Chemistry, University of Florence & INSTM, Via della Lastruccia 3, 50019 Sesto Fiorentino (FI), Italy

4 Department of Physics, University of Milan & CNR-IOM, Trieste, I-34149, Italy

5 Nanochemistry Department, Istituto Italiano di Tecnologia, Via Morego 30, 16163 Genoa, Italy

6 Department of Chemistry and Industrial Chemistry, University of Pisa, Via Moruzzi 3, 56124 Pisa, Italy

7 ICCOM-CNR, Sesto Fiorentino, Florence, I-50019, Italy

8 European Synchrotron Radiation Facility, 71 Avenue des Martyrs, 38000 Grenoble, Francia

9 Laboratory for Molecular Surfaces and Nanotechnology (LAMSUN), Department of Chemical Sciences, University of Catania and CSGI, Viale Andrea Doria 6, 95124, Catania, Italy

10 Department of Physics and Astronomy MS 61, Laboratory for Nanophotonics, Smalley-Curl Institute, Rice University, Houston, TX 77005, USA

\*corresponding author: gabriele.messina@iit.it

## ABSTRACT

We report the formation of  $\text{Au}_x\text{Ni}_{1-x}$  alloy nanoparticles obtained by pulsed laser irradiation of Au and Ni@NiO colloidal mixtures.

Structural and compositional characterization performed through X-Ray Diffraction and Transmission Electron Microscopy coupled with Energy Dispersive X-Ray Spectroscopy has shown a correlation between the final alloy composition and the different Au/Ni@NiO ratio in the irradiated mixture.

Supported by theoretical calculations, we propose as possible mechanism for the formation of the alloy structures a temperature increase and a subsequent melting of the structures, driven by the excitation of gold surface plasmon resonances.

Optical and magnetic characterization confirms a coexistence of the plasmonic and magnetic behaviors in the hybrid systems.

## 1.INTRODUCTION

Metallic alloy nanoparticles are attracting growing interest due to the possibility of combining the properties of the single metal components, thus allowing to obtain structures with new characteristics. In particular, great attention has been directed to magnetic nanoparticles because of their potential application in fields as optics, electronics, and medicine<sup>1, 2, 3</sup>. Unfortunately, magnetic metals such as iron, cobalt or nickel, which are often used for this purpose, are also prone to surface oxidation phenomena. For this reason, their combination with noble metals is desirable, since the latter ones maintain unaltered properties and present good resistance to corrosion and oxidation<sup>4, 5</sup>. A particularly promising alloy, in this framework, would be the one combining gold and nickel in a single nanostructure in view of the expected innovative applications such as in nanomedicine, information technology and catalysis<sup>6, 7, 8</sup>.

Several approaches for preparing  $Au_xNi_{1-x}$  nanocomposites have been reported in the past years, using both “wet” chemical synthesis as reverse microemulsions<sup>9, 10</sup> and physical routes like ion beam mixing<sup>11</sup> or electrodeposition<sup>12</sup>. Each of these approaches shows different problems: in the case of wet synthesis, the nanoparticles may present contaminated surfaces, while in the case of physical approaches, nanoparticles can be obtained only in the solid phase<sup>13</sup>.

Laser induced melting and mixing of metal nanoparticles in liquid media has demonstrated to be a good pathway for the formation of alloys<sup>14</sup>. In particular, the irradiation of gold with the Nd:YAG second harmonic has been used for the formation of Au-Ag alloys<sup>15, 16, 17, 18</sup>, Au-Zn<sup>19</sup>, Au-Cu<sup>20</sup> and Au-Fe<sup>21</sup>. Here we use laser mixing of nickel and gold nanoparticle dispersions in liquid media, in order to obtain  $Au_xNi_{1-x}$  alloys with different compositions by varying the Au/Ni nanoparticle ratio in the starting mixtures.

We also propose a physicochemical model, supported by theoretical temperature simulations, to explain the observed Au/Ni mixing behavior.

The alloy nanoparticles obtained by laser mixing in liquid are shown to maintain the optical and magnetic properties derived from both the starting metals, thus representing an outstanding base material for devices in which both properties are required.

## **2.EXPERIMENTAL DETAILS**

### **Laser ablation and irradiation**

Ablation was carried out with Au and Ni rods (99.99% purity by Goodfellow) in Millipore grade water.

The laser used for this work is a Nd:YAG laser with 10 ns pulse width and 10 Hz repetition rate (Continuum Surelite II).

### **XRD measurements**

Colloidal dispersion of the laser synthesized Au/Ni nanoparticles were deposited on Si <111>, and X-ray diffraction (XRD) measurements were performed with a Rigaku Ultima IV type III diffractometer, equipped with cross beam optics (CBO) by using a  $K\alpha$  wavelength emitted by a Cu anode. Careful alignment of source and detector with respect to the sample was reached by using a thin film attachment with three degrees of freedom. In order to avoid beam defocusing, the measurements were carried out in parallel beam mode. Divergence of the primary beam was reduced by a  $5^\circ$  Soller slit, while divergence of the diffracted beam was reduced by a  $0.5^\circ$  horizontal Soller slit. For grazing incidence XRD (GIXRD) measurements, the incident angle was kept at  $0.5^\circ$  to avoid any significant scattering from the substrates.

### **TEM characterization**

For transmission electron microscopy (TEM) analyses,  $\sim 50 \mu\text{L}$  of the nanocrystal suspensions were deposited onto carbon coated Cu grids. Overview bright field TEM (BF-TEM) and selected area electron diffraction (SAED) patterns were acquired using a JEOL JEM-1011 instrument with a thermionic W source operating at 100 kV. The SAED patterns were acquired at constant camera length after mechanically adjusting the height of the sample to the eucentric height and after carefully focusing the nanoparticle images. The corresponding diffraction camera length and the system distortions were calibrated using a nanocrystalline Au sputtered film on a standard C-covered Cu grid. The elaboration of SAED patterns (beam-stop removal, centering, azimuthal integration, and background subtraction) was carried out using the PASAD software<sup>22</sup>.

High-resolution TEM (HRTEM) and high angle annular dark field – scanning TEM (HAADF-STEM) analyses were performed using a JEOL JEM-2200FS microscope equipped with a Schottky

emitter operating at 200 kV and a CEOS spherical aberration corrector of the objective lens. Compositional analysis of the  $\text{Au}_x\text{Ni}_{1-x}$  alloy NPs was carried out by energy-dispersive X-ray spectroscopy (EDS) performed in STEM mode with a Bruker Quantax 400 system with a  $60 \text{ mm}^2$  silicon-drift detector (SDD). Quantification of the Au/Ni atomic ratio and of the oxygen content in the NPs was carried out using the Cliff-Lorimer ratio method for the Ni  $K\alpha$ , Au  $L\alpha$  and O  $K\alpha$  peaks in the collected EDS spectra.

### **XPS characterization**

X-ray photoemission spectroscopy analysis measurements were performed using a Kratos AXIS Ultra spectrometer with a basic chamber pressure in the range of  $10^{-9}$  Torr. The analysis was performed by using the Al  $K\alpha_{1,2}$  line at 1486,6 eV, with operating conditions of 10 KV and 15 mA. Emitted photoelectrons were analyzed with a hemispherical electron energy analyzer. Detailed spectra have been acquired with a resolution better than 1 eV.

### **UV-Vis characterization**

As prepared and mixed colloids (before and after irradiation) were analyzed with a UV-Visible spectrometer (JASCO V-650).

### **Magnetic characterization**

The magnetic properties of the nanoparticles were measured on dried samples using a SQUID magnetometer (Quantum Design MPMS XL-5). The magnetization versus temperature measurements were performed in zero-field cooled (ZFC) and field cooled (FC) conditions with a 50 Oe probe field. The hysteresis loops were measured at 300 K and 3 K with an applied field up to 5 T.

## **3. RESULTS AND DISCUSSION**

Au and Ni nanoparticles were separately produced by ablation of pure metal rods in water using the first harmonic of a 10 ns pulse width Nd:YAG laser. Ablation was carried out for 15 min at a fluence of  $30 \text{ J/cm}^2$ .

The final concentration of synthesized colloidal nanoparticles was estimated by weighing the metal targets before and after the ablation process. For both gold and nickel, a final concentration of  $\sim 10^{-6}$  M has been found.

In the case of nanoparticles prepared from a nickel target, XPS analysis (reported in Figure S1) showed the presence of a 60% of oxide on the particle. Such behavior is expected when working in an oxidizing environment like water.

Indeed, it has already been reported in literature that the ablation of a nickel target in water environment leads to the formation of Ni@NiO core-shell nanoparticles<sup>23</sup>.

The presence of an oxide shell can be related either to thermal oxidation of formed particles due to the aqueous vapor inside the cavitation bubble or to the presence of oxygen radicals in solution due to laser induced optical breakdown in water<sup>24</sup>. However, for the sake of simplicity, from now on we refer to these core@shell systems simply as nickel nanoparticles.

Gold and nickel freshly prepared colloidal solutions have then been mixed in different volume ratios (Au/Ni = 75/25, 66/33, 50/50 and 33/66) and irradiated with an unfocused beam (0.33 cm<sup>2</sup> diameter) using the second harmonic ( $\lambda=532$  nm) of the same Nd:YAG laser with a fluence of 0.2 J/cm<sup>2</sup> for 3 hours. Since single metal colloidal solutions present almost the same molar concentration, it can be assumed that the volume ratio corresponds to the effective molar ratio of the single metal particles in the mixture.

Figure 1 reports HAADF-STEM analyses of the irradiated sample Au/Ni 50/50 showing the presence of poly-disperse spherical nanoparticles (Fig 1a).

EDS analysis performed on the larger particles (30-40 nm diameter) shows a homogeneous distribution of Au and Ni within their volume, indicating the formation of an alloy structure (fig. 1b-c).

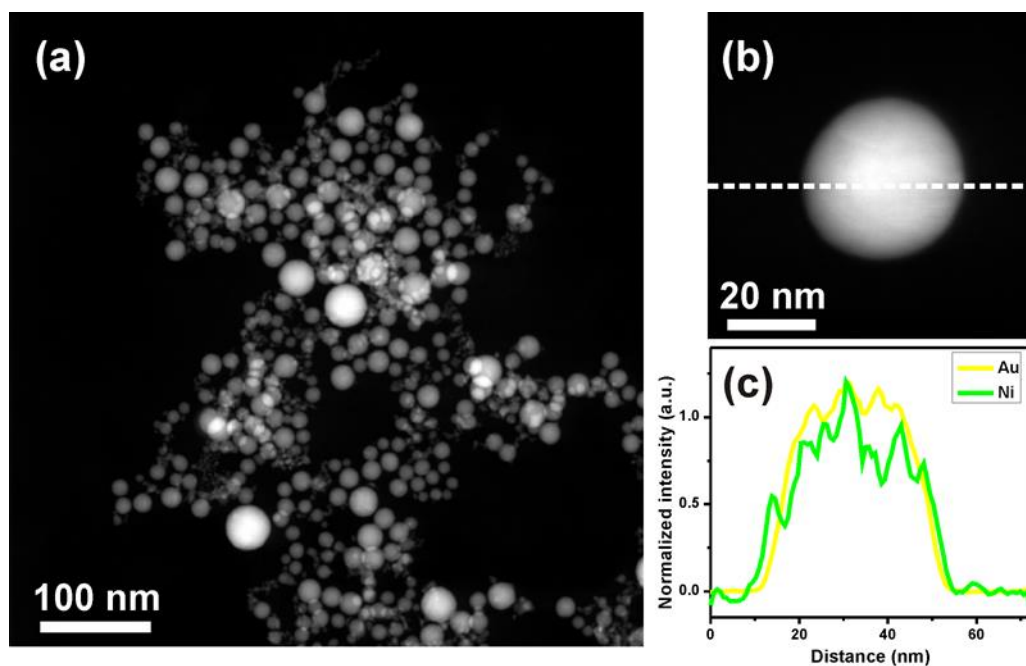


**Figure 1** (a) HAADF-STEM image of the colloidal mixture obtained from the 50/50 Au/Ni starting mixture. (b) Close-up on a representative larger particle. (c) Integrated intensities of Ni ( $K\alpha$ ) and Au ( $L\alpha$ ) EDS peaks across the particle shown in (b).

An atomic nickel percentage of around 10% was estimated by EDS quantitative analysis inside the larger nanoparticles, and no appreciable oxygen content was detected within larger particles in this sample.

However, the Ni content evaluated over large ensembles of small particles resulted of about 23% (fig. S2).

When analysing samples from starting mixtures with initial Au volume fraction equal to 66% and to 75% an average nickel atomic fraction of 6% and 7%, respectively, was found (see fig SI3 and SI4). In the case of larger particles of the Au/Ni 33/66 sample, a nickel atomic fraction of 26% was calculated by EDS. In addition, an oxygen atomic fraction ( $O/(Au+Ni+O)$ ) of 13% was evaluated. The HRTEM analysis evidences the presence of few nm-sized NiO domains inhomogeneously distributed on multiply twinned nanoparticles with crystal structure and cell parameters matching the ones of pure Au (Figure 2a). No evidence of NiO shell is obtained by EDS line scanning (Figure 2 b-c) due to the small size and inhomogeneous distribution of the NiO crystals on the particle surface.

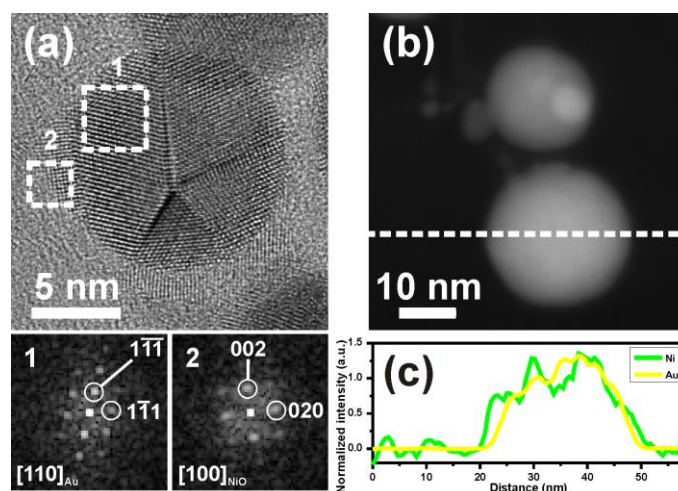
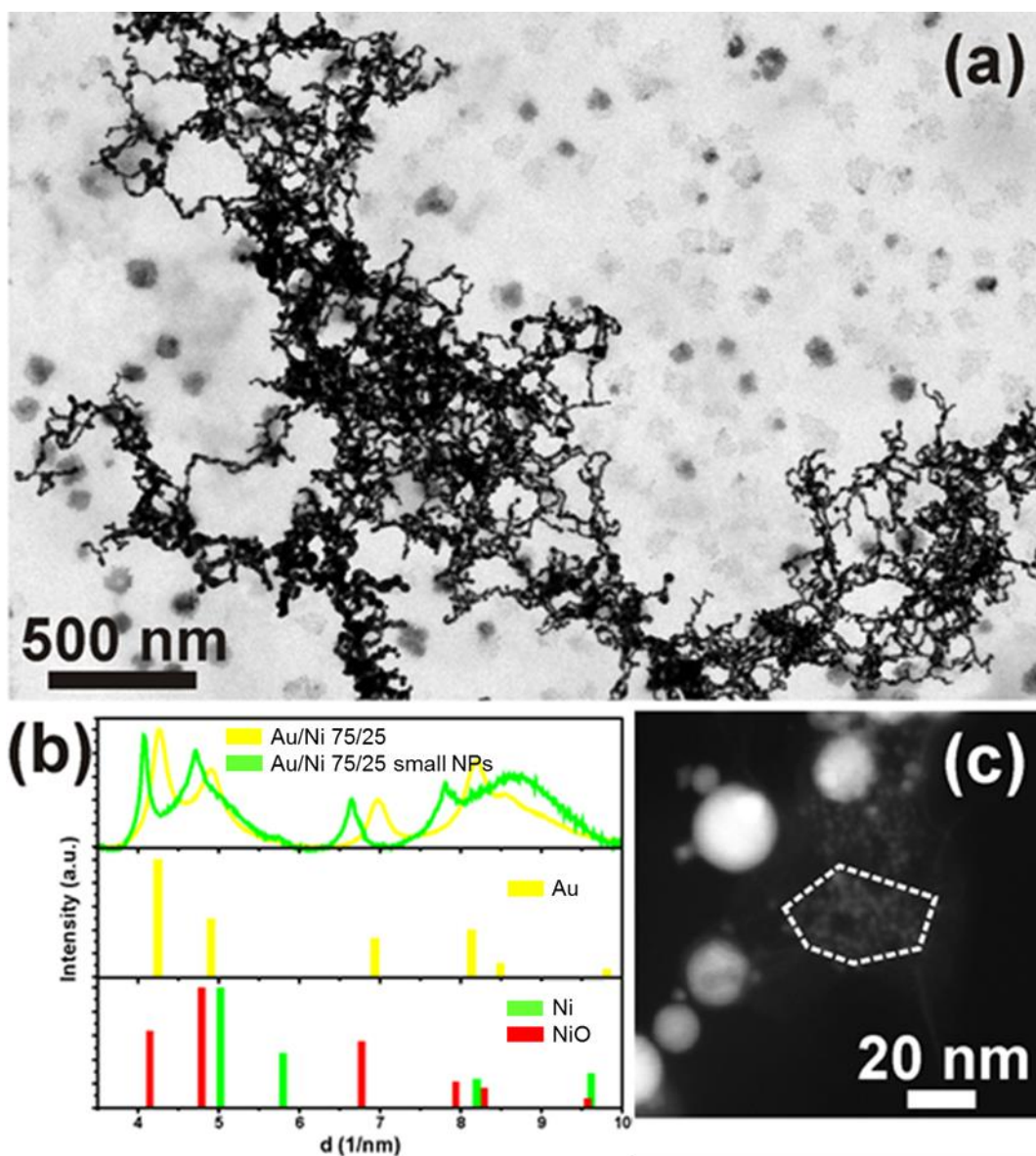


Figure 2. (a) HRTEM image of a particle in the sample obtained starting from a Au/Ni 33/66 mixture and (right) fast Fourier transforms obtained from two selected regions. (b) Integrated

intensities of Ni ( $K\alpha$ ) and Au ( $L\alpha$ ) EDS peaks across a particle from the sample (shown in (b) the corresponding HAADF-STEM image).

It is worth to note that Such analysis revealed that an increase of nickel in the starting mixture results in an increase of nickel in the final composition of the alloy.

In addition to larger the alloy particles ( $d=30-40$  nm), all the samples showed also the presence of smaller particles ( $d<10$  nm) and, in samples obtained from mixtures with high concentration of gold (Au/Ni 75/25 and Au/Ni 66/33), also ensembles with net-like shapes were found. SAED analysis performed on these structures, reported in Figure 3, revealed that the smaller particles exhibit a structure compatible with NiO, while net-like shapes present a pattern corresponding to pure gold.



**Figure 3.** (a) BF-TEM image and (b) corresponding azimuthally integrated SAED patterns obtained on the sample prepared starting with initial Au volume equal to 75% by selecting the net-like structures and the smaller nanoparticles. (c) HAADF-STEM image of the sample with the nominal Au fraction equal to 33%, showing a typical group of smaller nanoparticles, where the EDS atomic composition results to be Au:Ni:O=7:33:60.

The presence of gold particles forming chains is actually not surprising. Indeed, it is known that gold nanoparticles decrease their melting temperature as their size is decreasing<sup>25</sup>, so that, when irradiated undergo nanowelding phenomena<sup>26</sup>.

The effective formation of alloy structures has been further confirmed by XRD characterization, reported in Figure 4.

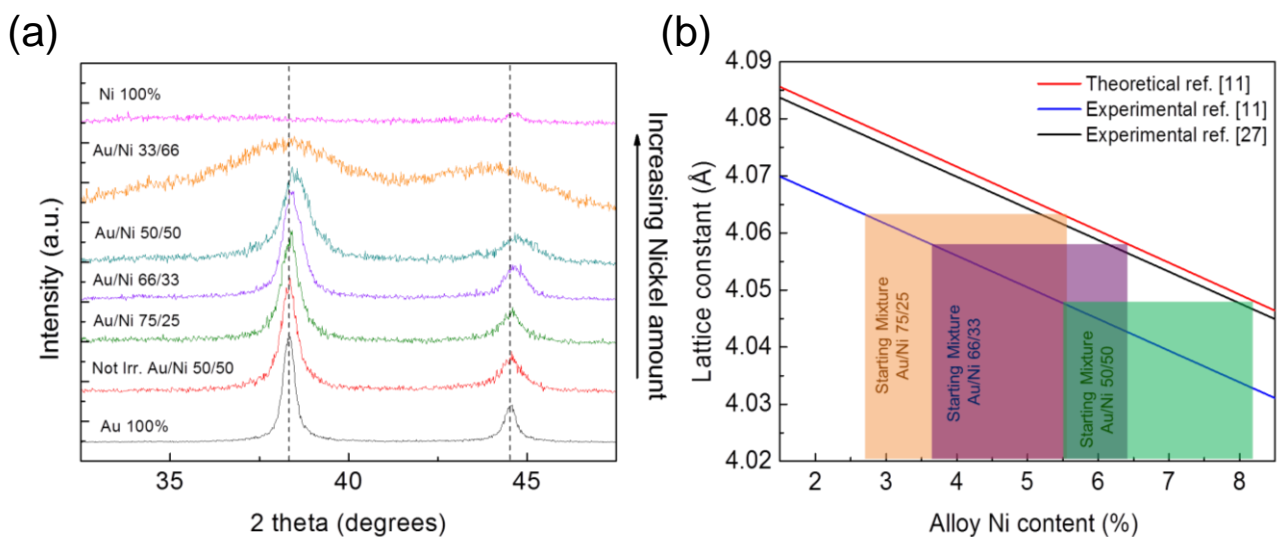


**Figure4.** (a) XRD measurements of pure gold and nickel nanoparticles and mixed alloys with different composition together with a mixture of non irradiated Au and Ni nanoparticles. (b) Lattice constant obtained from diffractograms in (a) as a function of the Ni atomic content in the initial

colloidal mixture for an Au/Ni alloys. Blue line and red line data from ref.11. Black line data from ref. 27. The trend over the whole Au/Ni percentage range can be found in fig. S5.

Indeed, patterns obtained from irradiated mixtures of gold and nickel colloidal solutions with different starting volume ratios showed a shift in Au (111) and (200) peaks (respectively at  $38.3^\circ$  and  $44.6^\circ$ ), when compared to samples containing only Au particles (black line in figure) and a non irradiated mixture of Au and Ni nanoparticles (red line in figure).

Such shifts can be related to a variation of the lattice constant parameter and indeed, by increasing the nickel amount, higher diffraction angles are recorded.<sup>9,10,12</sup>

In those cases where alloys are formed by metals presenting the same crystal structure and symmetry, Vegard's law theoretically predicts that the alloy should present cell parameters which are intermediate between the ones of the single components.<sup>11</sup> Since both pure Ni and Au occur in a face-centered cubic (fcc) structure (space group 225), with lattice constants  $3.45 \text{ \AA}$  and  $4.08 \text{ \AA}$ , respectively, their binary alloy is expected to have a fcc structure with intermediate lattice constant. Following the existing literature data, we have individuated a range of possible alloy compositions for each colloidal mixture. For instance the initial colloidal mixture Au/Ni=66/33, after irradiation, gives alloy nanoparticles with a range of nickel content 5.5-8%.(see fig. 4b)<sup>11,27</sup>

In the case of particles obtained from Au/Ni 33/66 starting mixture, diffractogram peaks are much broader, indicating the fragmentation of the nanoparticles into finely grained crystallites or the formation of an amorphous structure which does not allow to unequivocally define the peak position and then determine the amount of nickel from this kind of calculations.

A similar behavior has been already found in literature for the Ag-Cu system.<sup>28</sup>

These values, together with the ones obtained through EDS characterization, are reported in table 1 for comparison.

Initial Au/Ni volume fraction	Lattice constant (Å) as calculated by XRD	Au atomic percentage (XRD) after the irradiation	Au atomic percentage after irradiation (STEM-EDS) Larger particles	Au atomic percentage after irradiation (STEM-EDS) Smaller Particles
100/0	4.067	-	-	-
75/25	4.064	94.5-97.5%	96	93 (23% oxygen)
66/33	4.058	93.5-96.5%	94	94 (4% oxygen)
50/50	4.048	94.5-92.0%	91	77 (16% oxygen)
33/66	-	-	79	74 (13% oxygen)
0/100	-	-	-	-

**Table 1:** Lattice constants and composition of the  $Au_xNi_{1-x}$  nano-alloys derived from XRD and STEM-EDS methods.

The data in Table I show that compositions obtained through XRD are in good agreement with values obtained for the largest particle analysis by means of EDS, showing that the nickel percentage in the final alloy increases with the amount of nickel present in the starting mixture.

Therefore, the proposed alloying technique allows the tuning of the properties of the final product, by simply modulating the starting mixture composition.

### **Insight in Alloying mechanism: Nanoparticle temperature under irradiation**

In light of the above reported data, the following mechanism of nanoparticle alloying may be proposed.

We assume that the temperature increase of metallic nanoparticles (NPs) in solution depends both on the capability of the single NP to dissipate power and the overall density of the solution<sup>29,30,31</sup>. In our case, during the irradiation at  $\lambda=532$  nm, laser light is mainly absorbed by gold nanoparticles, due to its surface plasmon resonance (SPR). Moreover the Ni/Au phase diagram indicates that at temperature above 1100 K the two metals are miscible at any concentration<sup>32</sup>.

At the steady state condition, the final temperature at the surface of a spherical metallic nanoparticle placed in water, can be found analytically as<sup>29, 33</sup>,

$$T_{NP} = T_0 + \frac{P_{NP}}{4\pi\kappa_w R_{NP}}$$

where  $T_0$  is the ambient temperature,  $P_{NP} = \sigma_{acs}I$  is the power dissipated by the nanoparticle with absorption cross section  $\sigma_{acs}$  and incident intensity  $I$ ,  $\kappa_w$  is water thermal conductivity and  $R_{NP}$  is the radius of the NP.

Absorption cross sections have been determined using a FEM commercial software (COMSOL) where dielectric functions of Au and Ni have been fitted analytically<sup>34</sup>.

Absorption cross sections at  $\lambda = 532nm$  have been found to be:  $\sigma_{Au,acs} = 1.23 \cdot 10^{-16} m^2$  and  $\sigma_{Ni/NiO,acs} = 2.13 \cdot 10^{-17} m^2$  for 15 nm sized NPs.

In the case of Ni@NiO, only the core of the NP (11 nm size) is dissipating. As source, a  $w_0 = 1.5$  mm beam size pulsed laser with energy density  $E_d = 0.2 J/cm^2$ , pulse duration  $T_p = 10$  ns and repetition rate  $f_p = 10$  Hz has been chosen. Given Au and Ni diffusivities ( $a_{Au} = 127 \cdot 10^{-6} \frac{m^2}{s}$ ,  $a_{Ni} = 23 \cdot 10^{-6} \frac{m^2}{s}$ ), the single NP relaxation time ( $\tau_{Au} \approx \frac{R_{NP,Au}^2}{a_{Au}} = 0.4$  ps and  $\tau_{Ni} \approx$

$\frac{R_{NP,Ni}^2}{a_{Ni}} = 1.3$  ps) is much shorter than pulse duration:  $\tau_{Au}, \tau_{Ni} \ll T_p$ . Thus both for Au and Ni@NiO

NPs, the effective incident intensity can be calculated as  $I = \frac{E_d}{T_p} = 2 \cdot 10^{11} \frac{W}{m^2}$ , leading to single

NPs temperatures of:  $T_{NP,Au} = 728$  K and  $T_{NP,Ni} = 396$  K. Besides single NP dissipation one has to take into account also the average heating of the solution ( $T_{av}$ ) in order to find the final temperature reached by the nanoparticles [29]

$$T_{av} \approx 2.303 \frac{L_{opt} C_{NP} \sigma_{NP} P_{av}}{B \rho_w c_w V_w}$$

Here  $L_{opt} = 1$  cm is the optical length of the laser through the solution,  $C_{NP}$  is the particles concentration in the solution,  $\sigma_{NP}$  is the absorption cross section of the NPs,  $P_{av}$  is the average incident power (now the system relaxation time is much longer than pulse duration, thus  $P_{av} =$

$\pi w_0^2 E_d T_p f_p \approx 0.14 \text{ W}$ ),  $B \approx 0.12 \text{ s}^{-1}$  is the rate at which heat is released from the solution to the environment<sup>29</sup>,  $\rho_w = 10^3 \frac{\text{Kg}}{\text{m}^3}$  is the water density,  $c_w = 4.186 \cdot 10^3 \frac{\text{J}}{\text{Kg}\cdot\text{K}}$  is the water specific heat and  $V_w = 10 \text{ mL}$  is the solution volume.

Considering a solution with only Au nanoparticles with concentration  $C_{NP} = C_{Au} = 10^{-6} \text{ mol/L}$ , then the average temperature increase can reach values of  $\sim 50\text{K}$ . Thus the final temperature of gold nanoparticles in solution can be as high as:

$$T_{tot,Au} = T_{NP} + T_{av} \approx 780\text{K}$$

which is a temperature for which Au NPs may already enter a pre-melting phase<sup>35</sup>

Such calculations have been done for particles with size ranging from 15 to 30 nm and results are reported in Figure 5

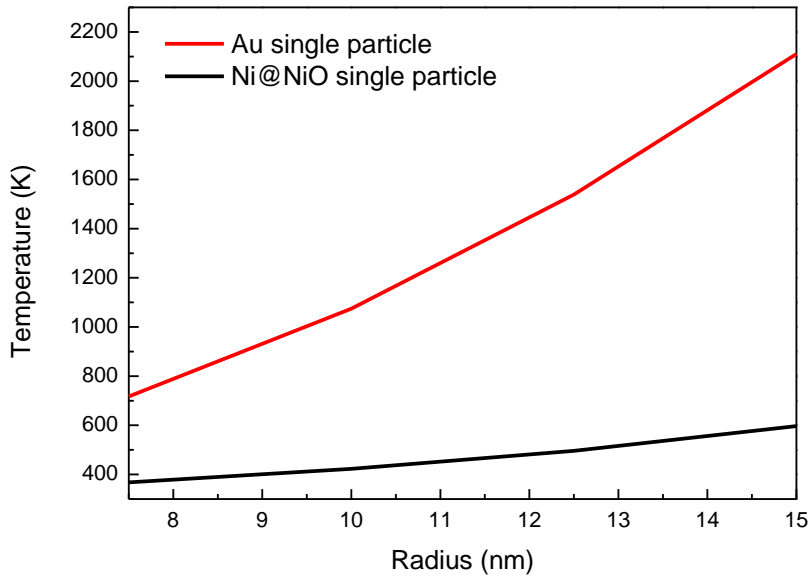


**Figure 5.** Temperature reached during laser irradiation at  $\lambda= 532 \text{ nm}$  (10 ns pulsewidth and 10 Hz repetition rate) by Au (red line) and Ni@NiO (black line) single particles as a function of their radius

While gold nanoparticles can reach a temperature of the order of 2000 K, Ni@NiO particles alone barely reach a temperature of around 600 K, which is lower than the value needed for the alloy formation.

This result supports the assumption that the alloying process is driven by a SPR related mechanism, as pictorially represented in Figure 6a.

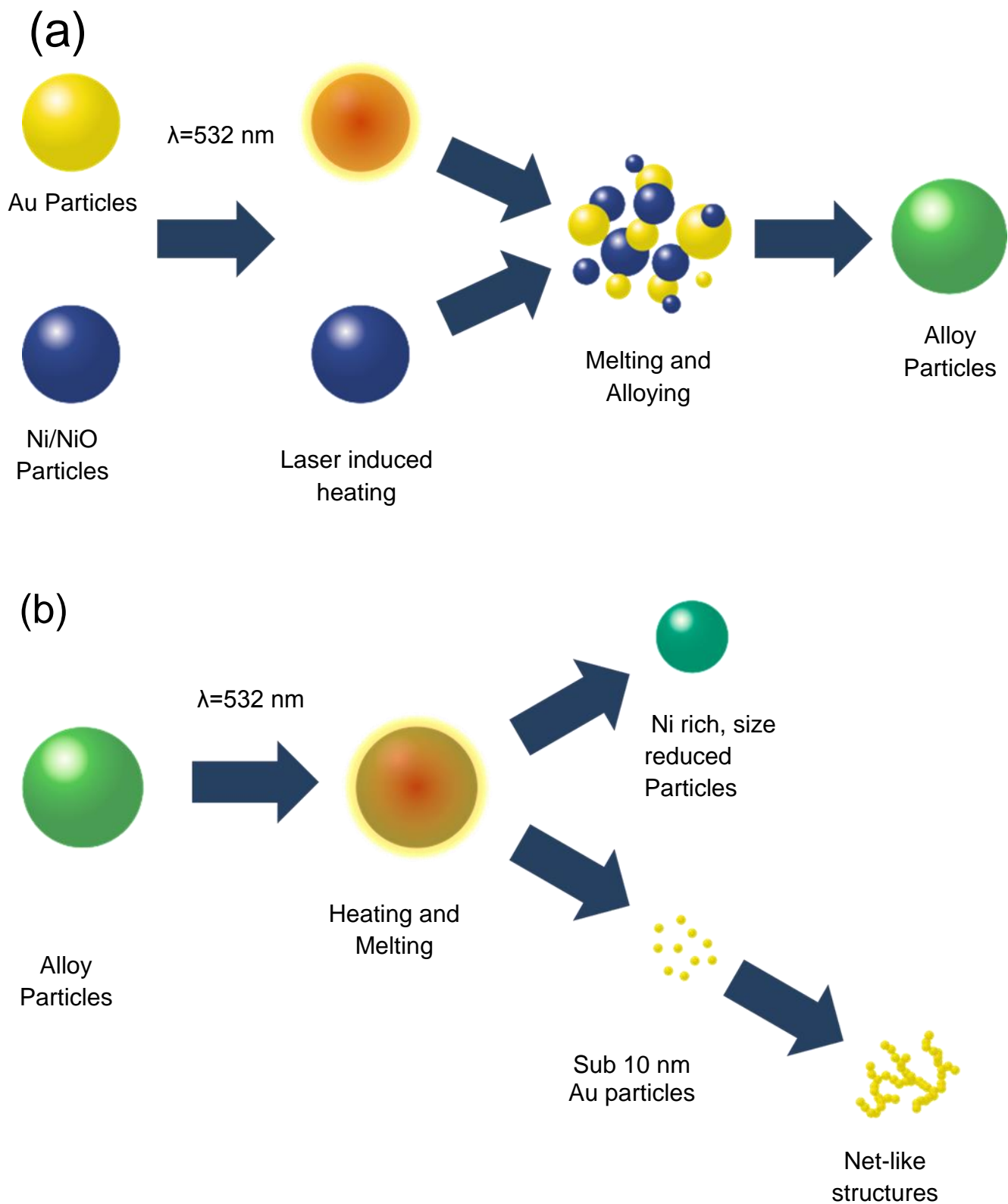


**Figure 6.** Schematic representation of the formation (a) and modification (b) of alloy nanoparticles.

In particular it should be noted that the larger the nanoparticle size, the higher the reached temperature. If we consider gold particles with a size of 15-20 nm, it is possible to reach temperatures that, according to the phase diagram, should allow the incorporation of nickel only in low percentage.

On the other hand, the incorporation of nickel leads to an increase in the particle size and therefore of the temperature that can be reached. In this way it is possible to overcome the temperature limit of 1100 K, above which there is total miscibility of the alloy phase.

At this stage of the alloy formation, kinetics will play a leading role. Indeed, in mixtures with higher concentrations of Ni@NiO NPs, the probability of collision and incorporation of nickel in forming alloy NPs will be higher.

The proposed model is also consistent with the presence of the additional side-structures found in the samples (schematically shown in Figure 6b).

One of the first observations is that smaller particles present a higher percentage of nickel with respect to bigger ones.

These particles cannot be formed during irradiation since, according to temperature calculations and the phase diagram, the incorporation of higher percentage of nickel should be penalized in the case of small particles.

Therefore, these particles should derive from post-irradiation of preformed larger particles.

As mentioned above, during irradiation, the gold SPR is resonant with the laser wavelength and this leads to absorption and heating. The excited system has to decay to lower energy state by melting and subsequent reduction of dimensions. Gold presents an enthalpy of melting of 12.55 kJ/mol, lower than that of nickel, which is 17.47 kJ/mol. This means that thermally excited alloy nanoparticles will find a favorable path to relax by losing gold atoms through melting, thus becoming smaller and richer in nickel.

Literature reports that fragmentation due to laser irradiation of nanoparticles is a phenomenon regulated by thermodynamics and thus the final size of the nanocrystals does not depend on parameters such as fluence or time of irradiation<sup>36</sup>. Such a process can be considered mainly thermal, since modification of gold due to charge accumulation through photoelectron emission and consequent breaking up can be considered negligible at 532 nm, being the work function of gold about 5.1 eV.<sup>37</sup>

A decrease in size determines a decrease of the temperature reached by the particle. When temperature is not high enough to allow the gold melting and expulsion processes, oxidation of nickel becomes competitive. However, the presence of gold, which has a lower valence than Ni(II),

should ideally decrease the oxidation rate of nickel. For this reason, bigger particles, which present higher amounts of gold, show lower oxidation rate on the surface<sup>38</sup>.

In contrast, particles with higher amount of nickel, as the ones obtained for the 33/66 mixture, are thermodynamically favored to oxidize, and therefore they will present an oxidized surface.

Finally, the small gold particles that are expelled from the bigger alloy nanoparticles, can weld together and form net-like shapes. The presence of a similar process has already been reported in the literature for gold NPs irradiated at resonant wavelength 26

The presence of such side-structures is responsible of the discrepancies between results obtained by XRD and EDS. While XRD spectra consider macroscopic portions of the sample, resulting in peak broadening, due to the small crystalline size of the gold net, and therefore overestimation of the gold percentage.

### Optical characterization

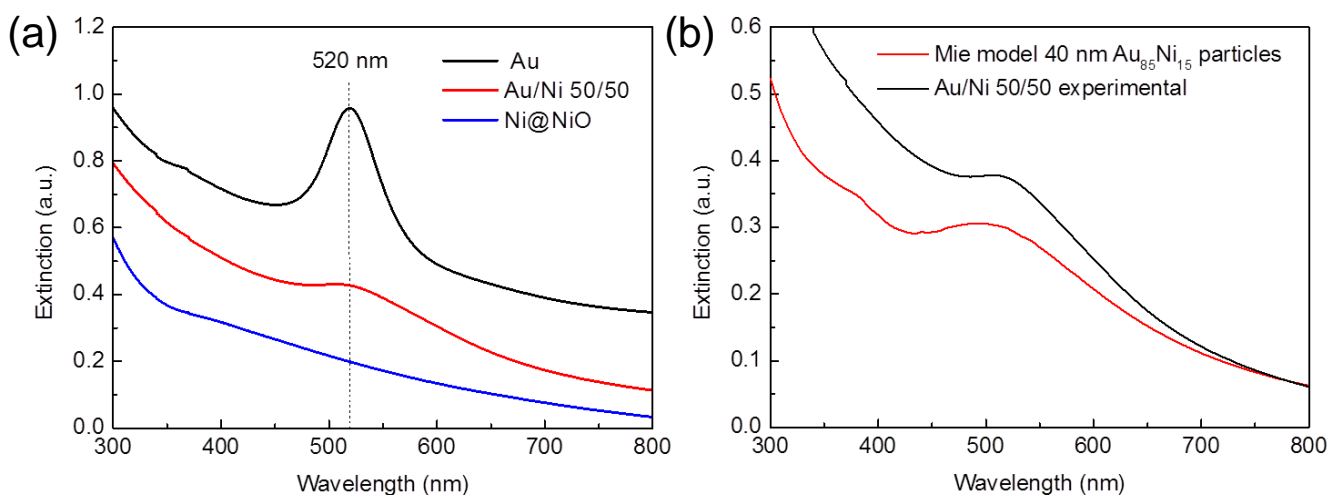


**Figure 7** (a) Extinction spectra of starting Au (black line) and Ni@NiO (blue line) mixture and of the irradiated 50/50 mixture (red line). (b) Experimental extinction spectrum of the 50/50 irradiated mixture (black) and spectrum calculated using Mie theory for a 40 nm diameter spherical nanoparticle using optical constants for a Au<sub>85</sub>Ni<sub>15</sub> alloy thin film from ref [39] (red line).

Figure 7a reports the extinction spectra of pure gold nanoparticles, of Ni@NiO nanoparticles and of the particle dispersion obtained irradiating a 50/50 starting mixture.

As expected, pure gold nanoparticles support the typical plasmon resonance at 520 nm, while Ni@NiO nanoparticles do not show any feature due to the plasmon damping of the NiO shell.

The irradiated mixture shows the presence of a very broad intensity plasmon resonance around 530 nm.

Similar damping of the plasmon resonance has been observed in the case of alloys obtained from the mixtures of other compositions (see figure S6) and can be related to the scattering of free electrons from the presence of lattice defects in the alloy. In order to analyze the origin of the behavior of the mixture, we should consider that, according to information from the TEM analysis, the solution is constituted mainly by sub 10 nm gold particles and larger alloy particles (approximately 40 nm).

It has already demonstrated that the optical behavior of spherical alloy nanoparticles can be described through Mie approximation using optical constants of bulk alloys [21].

Figure 7b shows the comparison between experimental extinction data for the sample Au/Ni 50/50 (alloy with composition  $\text{Au}_{90}\text{Ni}_{10}$ ) and theoretical simulation obtained using values of the dielectric function corresponding to a  $\text{Au}_{85}\text{Ni}_{15}$  thin film [39]

It is worth to note that the theoretical model seems to fit properly the experimental data, with the curve resembling the same shape and broadness of the SPR experimental spectrum.

The differences in intensity of the peaks can be related to the different composition of the experimental alloy with the one used as reference, which is richer in nickel.

Moreover, the experimental mixture presents also the contribution from small pure gold nanoparticles that have not been taken into account here.

## **Magnetic characterization**

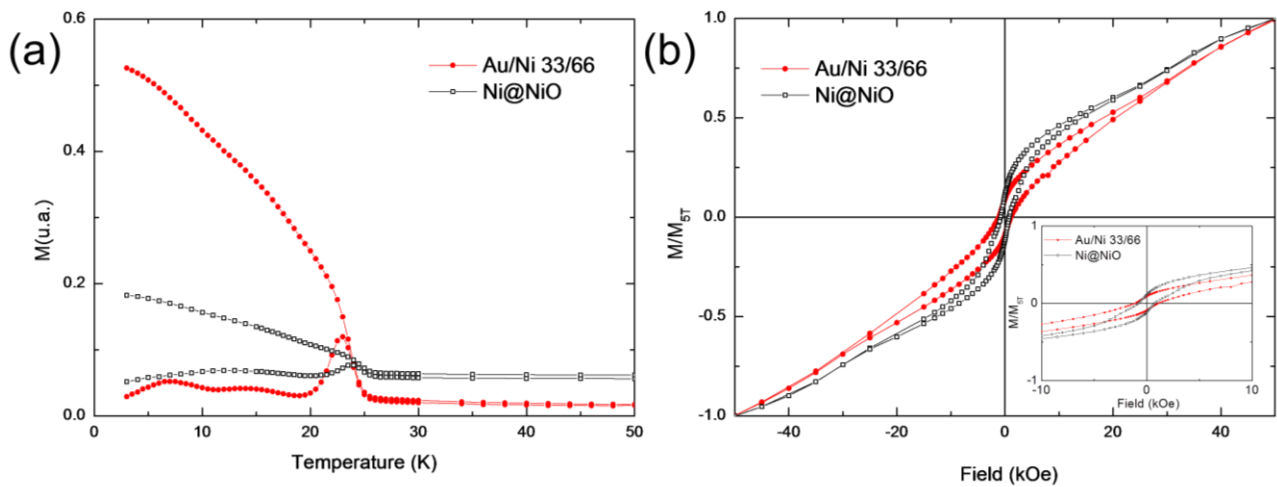
The magnetic response of the hybrid nanoparticles has been studied through a standard procedure, collecting the ZFC-FC curves and the hysteresis loops at room temperature (300 K), where a superparamagnetic response is expected, and at low temperature (3 K), where the nanoparticles are most likely blocked in a ferromagnetic state. The complex structure of these systems makes the analysis of the magnetic response particularly difficult, being the magnetic behavior the result of a convolution of all the magnetic components present in each sample. However, together with the evidence of a magnetic nature in these hybrid systems, a comparison of the several mixtures can be analyzed, confirming some aspects evidenced by the morphological and structural characterization.

Figure 8 shows the magnetic characterization of the Au/Ni 33/66 mixture compared to the starting solution of Ni@NiO nanoparticles, while the hysteresis loop at 300 K can be found in Figure S7. A correspondence can be found between the two specimens; in particular, the main peak at about 22 K

in the ZFC-FC curve of the 33/66 mixture recalls the same feature measured in the Ni@NiO sample. Such peak can be ascribed to the antiferromagnetic/paramagnetic transition of nanometric  $\beta$ -Ni(OH)<sub>2</sub>,<sup>40</sup> a likely byproduct of Ni oxidation in an aqueous environment. However, additional peaks at lower temperatures are evidenced in the ZFC-FC of the 33/66 system. They can be probably ascribed to additional smaller nanoparticle populations, or to the presence of small amounts of  $\alpha$ -Ni(OH)<sub>2</sub>.<sup>40</sup>

The 33/66 mixture shows a superparamagnetic response at room temperature, with a zero coercive field at temperatures above 22K, whereas the Ni@NiO system shows a residual hysteresis indicated by a slight irreversibility at higher temperatures (ZFC-FC in Figure 8) and confirmed by a coercivity (Hc) of about 100 Oe in the hysteresis loop at 300K (not resolvable from the inset Figure 8) and which can be ascribed to the presence of traces of macroscopic Ni@NiO which are blocked at room temperature.

On the other hand, the fact that at low temperature the magnetization does not saturate seems to confirm the presence of a low-temperature antiferromagnetic phase (such as  $\beta$ -Ni(OH)<sub>2</sub>), in line with ZFC-FC measurements.



**Figure 8** (a) ZFC-FC of the Au/Ni 33/66 mixture (full red dots) and the Ni@NiO nanoparticles (open black squares). (b) Hysteresis loops of the same samples measured at 3K. The inset is a zoom of the same hysteresis loops.

Analyzing the ZFC-FC curves of the Au/Ni 50/50 and 75/25 mixtures, a typical nanoparticle-like magnetic response emerges, with a  $T_B$  of about 12 and 11K, respectively. The coercivity of the hysteresis loop at 3 K is higher in the 50/50 specimen, reaching a value of about 1670 Oe. The behavior for both samples is compatible with an alloy nanoparticle system and it is reasonable to assert that one of the less intense peaks at low temperatures (below 22 K) visible in the ZFC-FC of the 33/66 mixture can be related to an alloy nanoparticles population similar to that one found in the 50/50 and 75/25 specimens.

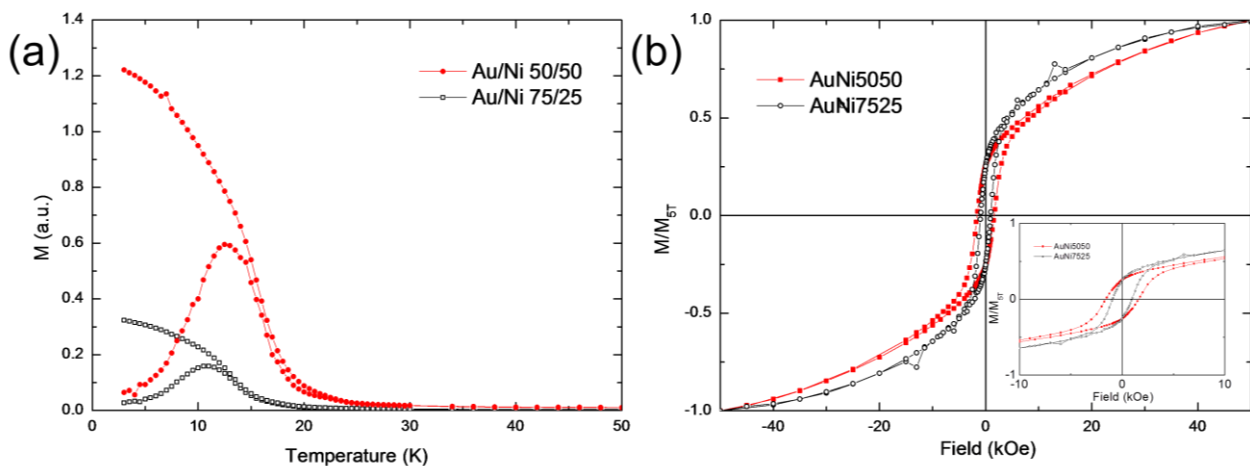


**Figure 9** (a) ZFC-FC of samples Au/Ni 50/50 (full red dots) and 75/25 (open blue squares). (b) Hysteresis loops of the same samples measured at 3K. The inset is a zoom of the same hysteresis loops.

To conclude, the magnetic characterization of this series of samples seems to indicate that for high Ni atomic ratios, antiferromagnetic phases resulting from the oxidation of Nickel in an aqueous environment are preponderant, while for higher Au atomic content, Ni oxidation seems to be mitigated by the formation of alloys and core-shell nanostructures.

## CONCLUSION

We have presented a technique for the formation of Au/Ni alloy nanoparticle based on SPR irradiation of colloidal mixture.

Structural characterization has shown that the ratio of different metal particles in the starting mixture can lead to the formation of alloy with increasing nickel atomic percentage at the increasing of nickel content in the starting mixture.

The optical and magnetic characterization supports the co-presence of plasmonic and magnetic properties, showing a dependence on the particle composition.

However a complex scenario takes place from the structural characterization, evidencing the presence of multiple populations including Ni@NiO nanoparticles and gold nets.

Supported by numerical simulations, we have proposed a model able to explain the formation of the alloy particles and the other side-structures found in the colloidal dispersions.

On the base of these results, we have demonstrated that laser irradiation is a technique able to tune the properties of the produced material, representing a green alternative to other synthesis “wet” techniques.

Moreover, the particularly clean surface of particles obtained through this approach allow their use in applications where high purity is requested, such as biosensing or photothermal applications.

## **ACKNOWLEDGEMENT**

The financial support from the European Research Council through the Advanced Grant “MolNanoMas” (267746) and from the Italian MIUR through FIRB projects “NanoPlasMag” (RBFR10OAI0) is acknowledged.

## REFERENCES

- 
- <sup>1</sup> S.H. Sun, C.B. Murray, D. Weller, L. Folks, A. Moser, *Science*, 2000, **287**, 1989
- <sup>2</sup> M. Spasova, V. Salgueiriño-Maceira, A. Schlachter, M. Hilgendorff, M. Giersig, L.M. Liz-Marzán, M. Farle, *J. Mater. Chem.*, 2005, **15**, 2095
- <sup>3</sup> S. Mornet, S. Vasseur, F. Grasset, E. Duguet, *J. Mater. Chem.*, 2004, **14**, 2161
- <sup>4</sup> Milton Stern, Herman Wissenberg, *J. Electrochem. Soc.* 1959, **106**, 759
- <sup>5</sup> N. D. Greenea, C. R. Bishop and M. Stern, *J. Electrochem. Soc.* 1961, **108**, 836
- <sup>6</sup> G. Armelles, A. Cebollada, A. García-Martín and M. Ujué González *Adv. Opt. Mat.* 2013, **1**, 10–35,
- <sup>7</sup> V. Bonanni, S. Bonetti, T. Pakizeh, Z. Pirzadeh, J. Chen, J. Nogués, P. Vavassori, R. Hillenbrand, J. Åkerman and A. Dmitriev, *Nano Lett.*, 2011, **11**, 5333
- <sup>8</sup> S. Panaro, A. Nazir, R. Proietti Zaccaria, L. Razzari, C. Liberale, F. De Angelis, and A. Toma *Nano Letters* 2015, **9**, 6128
- <sup>9</sup> D. Chen, S. Liu, J. Li, N. Zhao, C. Shia, X. Dua and J. Sheng, *J. Alloys Compounds*, 2009, **475**, 494
- <sup>10</sup> H.K. Chiu, I.C. Chiang and D.H. Chen, *J. Nanopart. Res.*, 2009, **11**, 1137
- <sup>11</sup> B.Y. Tsaur and M. Mäenpää, *J. Appl. Phys.*, 1981, **52**, 728
- <sup>12</sup> E. Rouya, G.R. Stafford, U. Bertocci, J.J. Malletta, R. Schad, M.R. Begleya, R.G. Kelly, M.L. Reede and G. Zangaria, *J. Electrochem. Soc.*, 2010, **157**, D396-D405

- 
- <sup>13</sup> S. Barcikowski and G. Compagnini, *Phys. Chem. Chem. Phys.*, 2013, **15**, 3022.,
- <sup>14</sup> G. Compagnini, E. Messina, O. Puglisi, V. Nicolosi, *Appl. Surf. Sci.*, 2007, **254**, 1007
- <sup>15</sup> Y.H. Chen and C.S. Yeh, *Chem. Commun.*, 2001, **4**, 371
- <sup>16</sup> A.T. Izgaliev, A.V. Simakin and G.A. Shafeev, *Quantum Electron.*, 2004, **34**, 47
- <sup>17</sup> A.T. Izgaliev, A.V. Simakin, G.A. Shafeev and F. Bozon-Verduraz *Chem. Phys. Lett.*, 2004, **390**, 467
- <sup>18</sup> G. Compagnini, E. Messina, O. Puglisi, R.S. Cataliotti and V. Nicolosi, *Chem. Phys. Lett.*, 2008, **457**, 386
- <sup>19</sup> F. Hajiesmaeilbaigi, M. Fazeli Jadidi and, A. Motamedi, *Acta Phys. Polonica A*, 2012, **121**, 59
- <sup>20</sup> M. Ganjali, M. Ganjali, S. Khoby, M.A. Meshkot, *Nano-Micro Lett.* 2011, **3**, 256
- <sup>21</sup> V. Amendola, M. Meneghetti, O. M. Bakr, P. Riello, S. Polizzi, D. H. Anjum, S. Fiameni, P. Arosio, T. Orlando, C. de Julian Fernandez, F. Pineider, C. Sangregorio and A. Lascialfari, *Nanoscale*, 2013, **5**, 5611
- <sup>22</sup> Gammer, C.; Mangler, C.; Rentenberger, C.; Karnthaler, H. P., Quantitative local profile analysis of nanomaterials by electron diffraction. *Scripta Materialia* **2010**, *63* (3), 312-315.
- <sup>23</sup> M.K. Singh, A. Agarwal, R.K. Swarnkar, R. Gopal and R.K. Kotnala *Sci. Adv. Mater.*, 2012, **4**, 532
- <sup>24</sup> C.A. Sacchi, *J. Opt. Soc. Am. B*, 1991, **8**, 337
- <sup>25</sup> P. H. Buffat and J. P. Borrel *Phys. Rev. A*, 1976, **13**, 2287
- <sup>26</sup> A. Poletti, G. Fracasso, G. Conti, R. Pilota and V. Amendola, *Nanoscale* 2015, **7**, 13702
- <sup>27</sup> E.C. Ellwood and K.Q. Bagley, *J. Inst. Metals*, 1951-1952, **80**, 617
- <sup>28</sup> K. D. Malviya and K. Chattopadhyay, *J. Phys. Chem. C* 2014, **118**, 13228
- <sup>29</sup> A. Alabastri, A. Toma, M. Malerba, F. De Angelis and R. Proietti Zaccaria, *ACS Photonics*, 2015, **2**, 115
- <sup>30</sup> H. H. Richardson, M. T. Carlson, M. T., P. J. Tandler, P. Hernandez, A. O. Govorov, *Nano Lett.* 2009, **9** (3), 1139
- <sup>31</sup> A. Alabastri, S. Tuccio, A. Giugni, A. Toma, C. Liberale, G. Das, F. De Angelis, E. Di Fabrizio and R. Proietti Zaccaria, *Materials* 2013, **6**, 4879
- <sup>32</sup> P. Franke, D. Neuschütz and Scientific Group ThermoData Europe, Binary Systems. Part 5: Binary Systems Supplement 1 2007, 19B5, 1 Springer Berlin Heidelberg

- 
- <sup>33</sup> G., Baffou, and H.Rigneault, Femtosecond-pulsed optical heating of gold nanoparticles. *Phys. Rev. B* 2011, **84**, 035415:
- <sup>34</sup> A.D. Rakic, A.B.. Djurisic, J.M.. Elazar and M.L; Majewski, *Appl. Opt.* 1998, **37**,, 5271
- <sup>35</sup> A. Plech, V. Kotaidis, S. Grésillon, C. Dahmen, G. von Plessen, . *Phys. Rev. B* 2004, **70**, 195423.
- <sup>36</sup> A. Takami , H. Kurita , and S. Koda *J. Phys. Chem. B* 1999, **103**, 1226
- <sup>37</sup> P.V. Kamat, M. Flumiani and G.V. Hartland, *J. Phys. Chem. B* 1998, **102** , 3123
- <sup>38</sup> R. Haugrud *Corrosion Science* 2003, **45**, 211
- <sup>39</sup> David J. McPherson, Supitcha Supansomboon, Benjamin Zwan, Vicki J. Keast, David L. Cortie, Angus Gentle, Annette Dowd, Michael B. Cortie, *Thin Solid Films* 2014, **551**, 200–204
- <sup>40</sup> David S. Hall, David J. Lockwood, Christina Bock, Barry R. MacDougall *Proc. R. Soc. A* 2015,**471**, 20140792